Comparison of Radar-Observed Tornadic and Nontornadic MCS Cells Using Probability-Matched Means

AMANDA M. MURPHY[a] AND CAMERON R. HOMEYER[a]

[a] *School of Meteorology, University of Oklahoma, Norman, Oklahoma*

(Manuscript received 28 April 2023, in final form 11 July 2023, accepted 30 August 2023)

ABSTRACT: Forecasting tornadogenesis remains a difficult problem in meteorology, especially for short-lived, predominantly nonsupercellular tornadic storms embedded within mesoscale convective systems (MCSs). This study compares populations of tornadic nonsupercellular MCS storm cells with their nontornadic counterparts, focusing on nontornadic storms that have similar radar characteristics to tornadic storms. Comparisons of single-polarization radar variables during storm lifetimes show that median values of low-level, midlevel, and column-maximum azimuthal shear, as well as low-level radial divergence, enable the highest degree of separation between tornadic and nontornadic storms. Focusing on low-level azimuthal shear values, null storms were randomly selected such that the distribution of null low-level azimuthal shear values matched the distribution of tornadic values. After isolating the null cases from the nontornadic population, signatures emerge in single-polarization data that enable discrimination between nontornadic and tornadic storms. In comparison, dual-polarization variables show little deviation between storm types. Tornadic storms both at tornadogenesis and at a 20-min lead time show collocation of the primary storm updraft with enhanced near-surface rotation and convergence, facilitating the nonmesocyclonic tornadogenesis processes.

KEYWORDS: Severe storms; Squall lines; Tornadoes; Radars/radar observations

1. Introduction

Improving the predictability of tornadoes and tornadic storms is crucial to the National Weather Service mission statement of protecting life and property (Uccellini and Ten Hoeve 2019). From 1986 to 2011, tornadoes for which warnings were issued in advance had an average lead time of 18.8 min, and the total frequency of such advanced warnings increased from approximately 25% in 1986 to more than 50% in recent years (Brooks and Correia 2018). Tornado probability of detection (POD; i.e., warned in advance of occurrence) is greater than 80% for tornadoes from supercells but less than 50% for tornadoes from nonsupercellular storms, which are warned on average ~2 min later than supercellular tornadoes and are 3 times as likely to be warned at negative lead times (i.e., after the time of tornadogenesis; Brotzge et al. 2013). Nonsupercellular tornadoes are produced not by a persistently rotating mesocyclonic storm, but rather by the tilting of vorticity into the vertical by updrafts or downdrafts to create counterrotating mesovortices at the leading edge of a storm (e.g., Weisman and Davis 1998; Trapp and Weisman 2003; Flournoy and Coniglio 2019). In particular, Flournoy and Coniglio (2019) and Gibbs (2021) note in their reviews of quasi-linear convective system (QLCS) tornadogenesis that line-normal low-level shear plays an important role in mesovortex genesis for QLCSs when cold pool and updraft strength are sufficiently balanced by Rotunno–Klemp–Weisman theory (see also Weisman and Trapp 2003; Rotunno et al. 1988). Knowing that QLCS storms are a type of mesoscale convective system (MCS; e.g., Agee and Jones 2009), there is clear incentive to examine methods to improve nonsupercellular MCS tornado warnings.

Climatological studies have found that anywhere from 18% to 27% of tornadoes are associated with MCSs or QLCSs (Trapp et al. 2005; Ashley et al. 2019; Murphy et al. 2023). Murphy et al. (2023) also found that approximately one-half of subsignificant severe tornadoes were associated with MCSs, and MCSs accounted for the majority of tornado-producing storms during the overnight hours. Nighttime tornadoes can pose a greater threat to life and property since people are asleep and are least confident in their ability to receive warnings even when a tornado is detected at positive lead times (Krocak et al. 2021). The negative impacts of a low POD for nonsupercell QLCS storms are likely to only amplify with time, since the proportion of QLCS-attributed tornadoes is increasing (Ashley et al. 2019). Acknowledging that improved warnings do not operate in a vacuum and that any behavioral response to warnings is impacted by both meteorological and social factors (e.g., Agee and Jones 2009; Hoekstra et al. 2011; Mason et al. 2018; Ripberger et al. 2019; Ernst et al. 2021; Trujillo-Falcón et al. 2021), greater understanding of how MCS nonsupercellular tornadoes form and what storm and environmental factors delineate a tornadic from a nontornadic MCS cell can aid in improving warning metrics and saving life and property.

Often, attempts to nowcast a storm's tornadic potential rely on local environmental analyses and comparisons with historical environmental analogs. Coffer et al. (2019) note that such analyses go back as far as the 1940s and 1950s, with modern techniques for analyzing storm environments mainly relying on model-derived proximity soundings given the relative dearth of proximity soundings near severe and/or tornadic storms. Thompson et al. (2012) examined differences between QLCS and right-moving supercellular tornado environments

Corresponding author: Amanda M. Murphy, amanda.murphy@ou.edu

DOI: 10.1175/JAMC-D-23-0070.1

using hourly Rapid Update Cycle (RUC) analysis data, finding that "environmental differences between the supercells and linear modes were relatively small." Anderson-Frey et al. (2016) also examined QLCS and right-moving supercellular tornadic environments using RUC data, again finding a great deal of overlap between supercellular and QLCS tornadic environments' derived parameters. In addition to overlap in environments for various storm modes, hits and misses for tornado warnings within environmental parameter spaces of each storm mode also have considerable overlap, "perhaps highlighting the difficulty in distinguishing between storms that will be tornadic and those that will not be tornadic in similar environments" (Anderson-Frey et al. 2016). Lyza et al. (2022) note in their analyses of supercells during the April 2011 tornado outbreak that tornado-producing supercells were occasionally located near "dormant" cells, motivating the need to look beyond storm background environments and toward storm-scale environmental heterogeneities and "internal stochastic processes of supercells" to determine whether or not a storm will produce a tornado. In addition, environmental reanalysis data have shown limitations in representing the low-level environment of storms (Taszarek et al. 2021; Coniglio and Jewell 2022), reducing their utility for tornadogenesis prediction.

Another way to anticipate potential tornadogenesis is by analyzing a storm's presentation on radar and comparing it with historical radar data. While not inherently a predictive tool, weather radar can give insight into storm dynamics and physics, thereby helping to determine if a storm is developing in a manner consistent with past tornadic storms. The WarnOn Forecast program (Stensrud et al. 2009, 2013) has used simulated radar reflectivity along with other model parameters to attempt to forecast which storms may become tornadic in the next few hours. Skinner et al. (2018) showed that such studies' average forecast critical success index (CSI or "skill"; Schaefer 1990) ranged from 0.7 at 20-min forecast times to 0.4 at near-3-h forecast times, an increase over the expected baseline CSI of ~0.2–0.3 (Anderson-Frey and Brooks 2021). Focusing on observed radar signatures, Homeyer et al. (2020) analyzed hundreds of tornadic and nontornadic supercell storms in the United States to elucidate common radar signatures of both types of storms, both at peak intensity and at 20-min lead times. Using a probability-matched mean (PMM) approach, which produces maps of average storm radar moments and/or variables at selected altitudes without artificially dampening the full range of values typical of each individual storm (Ebert 2001), they found tornadic supercell storms have increased vertical alignment of the mesocyclone and differing orientation of low-level polarimetric radar signatures relative to the direction of storm motion. The aforementioned study by Lyza et al. (2022) also looked at radar characteristics of supercells and found that mean azimuthal shear (rotation) discriminated well between nontornadic, pretornadic, and tornadic supercells. These studies on how radar observations of supercells relate to tornado potential motivate applying a similar technique to nonsupercell storms. For example, Loeffler and Kumjian (2018) examined low-level differential reflectivity Z_{DR} and specific differential phase K_{DP} signatures in tornadic and nontornadic nonsupercell storms with varying storm modes, finding statistically significant differences in the way the maxima of the two were oriented relative to storm motion in tornadic as compared with nontornadic storms. By examining the radar presentation of nonsupercell MCS storm cells specifically, potential differences between tornadic and nontornadic cells can be elucidated for improved short-term forecasting and nowcasting of tornadoes.

Herein, we present a PMM analysis of thousands of tornadic and nontornadic nonsupercellular MCS storm cells identified in the 10-yr GridRad-Severe dataset to determine if there are radar signatures that enable discrimination between storm types at both peak intensity and at a given lead time to first tornadogenesis. We first summarize the technique used to identify an appropriate null population of nontornadic storms. Differences in PMM fields of radar variables and moments are then evaluated at multiple altitudes above ground level (AGL) for each storm type. These signatures are summarized, and directions for future research are discussed.

2. Data and methodology

a. GridRad-Severe data

For all analyses in this study, the GridRad-Severe (GR-S; Murphy et al. 2023) dataset is used. GR-S includes gridded radar data from the U.S. NEXRAD WSR-88D S-band radar network with single-polarization data from 2010 to 2012 and dual-polarization (or polarimetric) data starting in 2013 (Crum and Alberty 1993). For each year in the original 10-yr database (2010–19), approximately 100 high-end severe weather days are selected, and radar data from a flexible spatiotemporal domain are gridded to a regular latitude–longitude–altitude grid at 5-min intervals. The grid has a longitude–latitude resolution of 48 grid points per degree (~0.02°) and an altitude resolution of 0.5 km at and below 7 km above mean sea level (MSL) and 1 km at higher altitudes of up to 22 km MSL. All years include radar reflectivity at horizontal polarization Z_H, Doppler velocity spectrum width σ_V, azimuthal shear of the radial velocity (rotation), and radial divergence of the radial velocity. Years with polarimetric data also include Z_{DR}, K_{DP}, and copolar correlation coefficient ρ_{HV}. These variables were selected for analysis given the microphysical and kinematic insights that can be drawn from them. These include hydrometeor size, shape, and concentration (Z_H, Z_{DR}, and K_{DP}); particle type and/or orientation diversity (ρ_{HV}); radial motion and variability in radial motion (azimuthal shear and σ_V); and local vertical motion (radial divergence). More discussion on these variables can be found in Homeyer et al. (2020). Each GR-S event includes objective storm tracks based on 30-dBZ echo-top maxima, and radar volumes are extracted along the GR-S storm tracks for PMM analysis herein. This 30-dBZ echo-top tracking was used instead of 40-dBZ echo tops (as in Homeyer et al. 2020) since these data span the entire calendar year, and storms are often weaker in the fall and winter months. A lower echo-top threshold ensures that off-season storms are not missed by the tracking algorithm. We have found that the location of the 30-dBZ echo-top maximum differs minimally from the location

of the 40-dBZ echo-top maximum when both are present (not shown). In addition, the storm tracks are objectively matched with nearby storm reports for severe storm identification. Other storm properties, such as storm mode and supercell classification, are derived from the data to enable isolation of MCS nonsupercell storm cells in this study. Additional detail on the creation of GR-S data is available in Murphy et al. (2023).

As in Murphy et al. (2023), MCS cells are defined as storm tracks embedded within a 30-dBZ column-maximum reflectivity contour with at least one additional tracked storm, so long as the maximum dimension of the 30-dBZ contour is $\geq$ 100 km. If a 30-dBZ contour encompasses only two tracked storms, the contour area must also be $\geq$ 3000 km^2 for any enclosed storms to be classified as MCS cells (to avoid misclassification of isolated, cycling supercells). Supercells are classified via a collection of kinematic characteristics outlined in Murphy et al. (2023) based on Homeyer et al. (2020) and Sandmæl (2017), including measurements of azimuthal shear, radial divergence, and spectrum width. We identify supercells to exclude them from analysis of nonsupercellular MCS cells in this study, of which there are 1627 tornadic and 357 741 nontornadic cells. Of those, 1166 tornadic and 240 536 nontornadic occurred during or after 2013, when polarimetric data are available.

b. *Selecting tornadic and null populations*

Tracked storms identified as nonsupercellular MCS cells for ≥75% of their lifetime are isolated for analysis. This 75% threshold aims to focus attention on cells that are predominantly classified as MCS cells while also allowing for some variation in mode classification during their life cycles. These nonsupercell MCS storm cells are further split into tornadic and nontornadic populations based on whether they were linked with a tornado report at any point in their lifetime. Sensitivity tests to the MCS lifetime threshold spanning 50%–100% were carried out and resulted in fairly similar bulk population characteristics. In particular, regardless of the threshold chosen, the degrees of separation between tornadic and nontornadic distributions were fairly similar, with Kolmogorov–Smirnov (K–S) significance tests differing by a median of ~8% when examining distributions of lifetime maximum, median, and minimum values of radar metrics for different MCS lifetime thresholds. A less restrictive threshold was ultimately preferred to maximize sample size.

Identifying differences between tornadic and nontornadic storms, especially in the time before first tornadogenesis, is incredibly important for warning applications. Comparing these two populations without any further processing would be informative; however, the main challenge for improving warning metrics for nonsupercellular MCS storms comes from identifying nontornadic storms that otherwise look promising for tornadogenesis and comparing their characteristics with those of tornadic storms. Using radar data, we can further identify unique storm characteristics that may separate these populations. Radar characteristics used to select nontornadic storms that have similar characteristics to tornadic storms—that is, the null population—include azimuthal shear, radial divergence, and spectrum width over various layers, as well as vertically integrated liquid water content (VIL density, a metric for severe hail potential; Greene and Clark 1972; Amburn and Wolf 1997) and low-level hail differential reflectivity H_{DR} (a polarimetric metric for severe hail potential; Aydin et al. 1986). These data are examined over both low-level (LL; $0 \leq z < 4$ km AGL) and midlevel (ML; $4 \leq z \leq 7$ km AGL) layers, and column-maximum values are also examined. For each storm, the median value of each variable across the entire storm's lifetime is retained for comparison. Figure 1 shows the distributions of these variables for tornadic and nontornadic storms. Median data are used instead of storm lifetime maximum or minimum values because results of K–S significance tests to assess differences in the distributions were typically higher for storm lifetime median values. It is possible that this result arises due to mitigation of the influence of spurious features and tornadic circulations by using a median filter.

The degree of separation between the nontornadic and tornadic nonsupercellular MCS cell populations for each variable is quantified to determine which best delineates between storm types. Null storms can then be selected from the smaller population of nontornadic storms that overlap the distribution of tornadic cell values for variables with a high degree of separation, since such storms would be most likely to be (incorrectly) warned as potentially tornadic. To quantify the significance of separation between the tornadic and nontornadic distributions, K–S and two-sample t tests were performed. The t tests show that all variables exhibited a significant difference ($p < 0.05$) between the tornadic and nontornadic distributions. K–S tests, with values calculated from normalized CDFs, showed that maximum ML azimuthal shear (0.07), maximum LL azimuthal shear (0.07), maximum column-maximum azimuthal shear (0.06), and maximum LL divergence (0.04) had the largest K–S values of all variables and therefore showed the largest separation between tornadic and nontornadic storms. Maximum LL H_{DR} (0.07) also had one of the largest K–S test values, but given that it could not be calculated for storms from 2010 to 2012, it was not considered as a criterion for null case selection.

Of the identified radar-derived variables with high K–S test values, null storms are selected using LL azimuthal shear values, since high LL azimuthal shear values are often interpreted as anecdotal radar evidence of a mesovortex capable of producing a tornado. Using the histogram of tornadic LL azimuthal shear values in Fig. 1, null storms are randomly sampled from the nontornadic distribution at the observed frequency of tornadic storms. The resulting null sample exhibits an equivalent LL azimuthal shear distribution to the tornadic sample and enables confident comparison of storms that differ nearly solely by their tornadic production. Figure 2 shows the distribution of tornadic and null storms for the nine variables shown in Fig. 1. Two of the 1627 tornadic storms did not have LL azimuthal shear data, so the null sample is 1625 storms. Sensitivity testing demonstrates that null distributions in Fig. 2 do not change meaningfully with varying random samples (not shown).

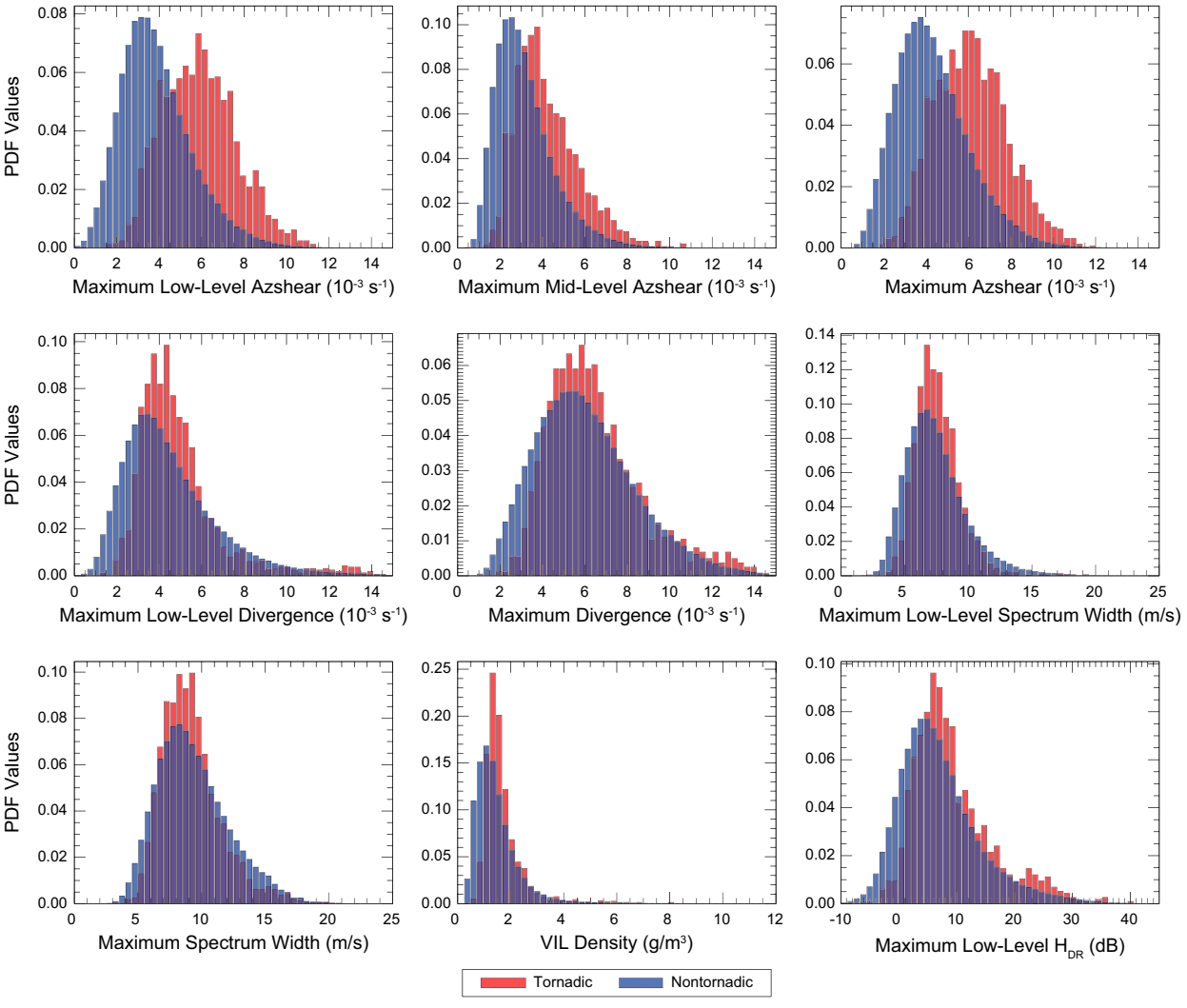

FIG. 1. Distributions of kinematic variables for tornadic and nontornadic nonsupercellular MCS storms within the GR-S dataset from 2010 to 2019, inclusive. Data are the median values of the listed radar variable across each storm's lifetime.

c. *Probability-matched mean technique*

After identifying tornadic and null storms, PMMs of radar data for each population are created. Similar to the work in Homeyer et al. (2020), PMMs show the average spatial distribution of a given radar variable with values scaled to avoid nonphysical smoothing due to the averaging process. These data differ in that the focus herein is on nonsupercellular MCS storms, as compared with Homeyer et al. (2020)'s analyses of supercell storms. Examining storm-average appearances in this way highlights the signatures within tornadic or nontornadic storms that show up most consistently ("repeatable and substantial differences"; Homeyer et al. 2020), emphasizing the most robust distinctive features within tornadic and nontornadic storms and screening out less consistent storm-to-storm variabilities. PMMs are created at 0.5, 1.5, 3, 5, and 10 km AGL for Z_H, azimuthal shear, radial divergence, and σ_V for all cases, and Z_{DR}, K_{DP}, and ρ_{HV} for storms with polarimetric data (2013 and later). Tornadic storms are analyzed at 0 and 20 min prior to first tornadogenesis, and null storms are analyzed at times of peak 30-dBZ echo-top height and peak LL rotation. These two times within the null storms' lifetimes are selected to focus on the time of peak storm intensity (and presumed strongest updraft) and strongest low-level circulations, respectively. Both times aim to isolate the most likely time for tornadogenesis via stretching of low-level vorticity (Markowski and Richardson 2009). Similar to Homeyer et al. (2020), extreme values from the individual storm observations are trimmed before computing the PMMs. Extrema in this study are considered to be values less than the 0.1th and greater than the 99.9th percentile of all observations contributing to a PMM (as in Homeyer et al. 2023). For single-polarization analyses, 1625 null and 1627 tornadic storms are analyzed, respectively; for dual-polarization analyses, these numbers are reduced to 1231 and 1166 storms (an approximate reduction of ~25%). A total of 840 and 621 of the 1627 tornadic storms could be

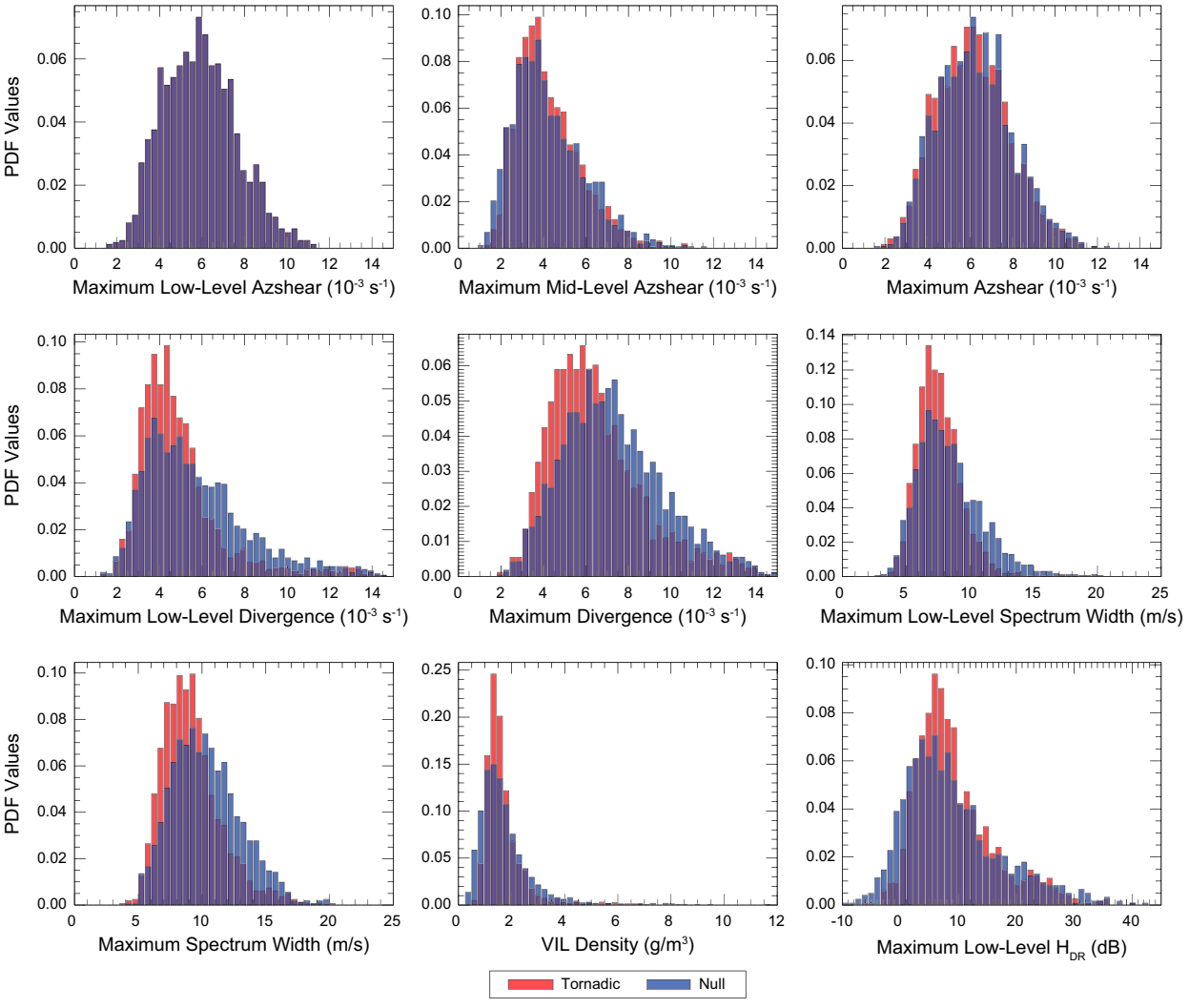

FIG. 2. As in Fig. 1, but comparing tornadic storms with the sampled null storms.

tracked at 20-min lead times for single- and dual-polarization analyses, respectively. By creating and comparing PMMs of tornadic and null storms, further differences may be revealed and highlighted between these two populations.

3. Results

a. Single polarization

Single-polarization radar variables lend insight into the difference between null and tornadic storms at and before their peak intensity. Figure 3 shows storm-centered, constant-altitude PMMs of Z_H for null and tornadic storms. Individual storm observations are centered on each storm's maximum 30-dBZ echo-top location and rotated such that storm motion points to the right before PMMs are calculated. When discussing features of any individual PMM plot, signatures and their locations are all described relative to storm center and storm motion, to ensure clarity. The primary differences between the null and tornadic data in Z_H are in the mean storm shape: null storms have more of a diffuse, circular shape when compared with tornadic storms (in both times analyzed), which have higher reflectivity more tightly aligned on a lower-left to upper-right axis (relative to storm motion). This may indicate a more consistent MCS line orientation relative to storm motion for tornadic storms when compared with null storms. Panels of tornadic storm data at tornadogenesis also show contoured frequency of tornado reports, which are offset slightly right of storm motion and up-motion relative to storm center (i.e., the echo-top maximum).

Investigations of azimuthal shear, radial divergence, and σ_V PMMs show how the location of common storm-relative features differs between null and tornadic storms. Figure 4 shows storm-centered, constant-altitude PMMs for azimuthal shear. A key feature present in all PMMs is a mesovortex (quasi elliptical, highly positive values) right of storm motion and displaced up to 10 km from storm center. For tornadic

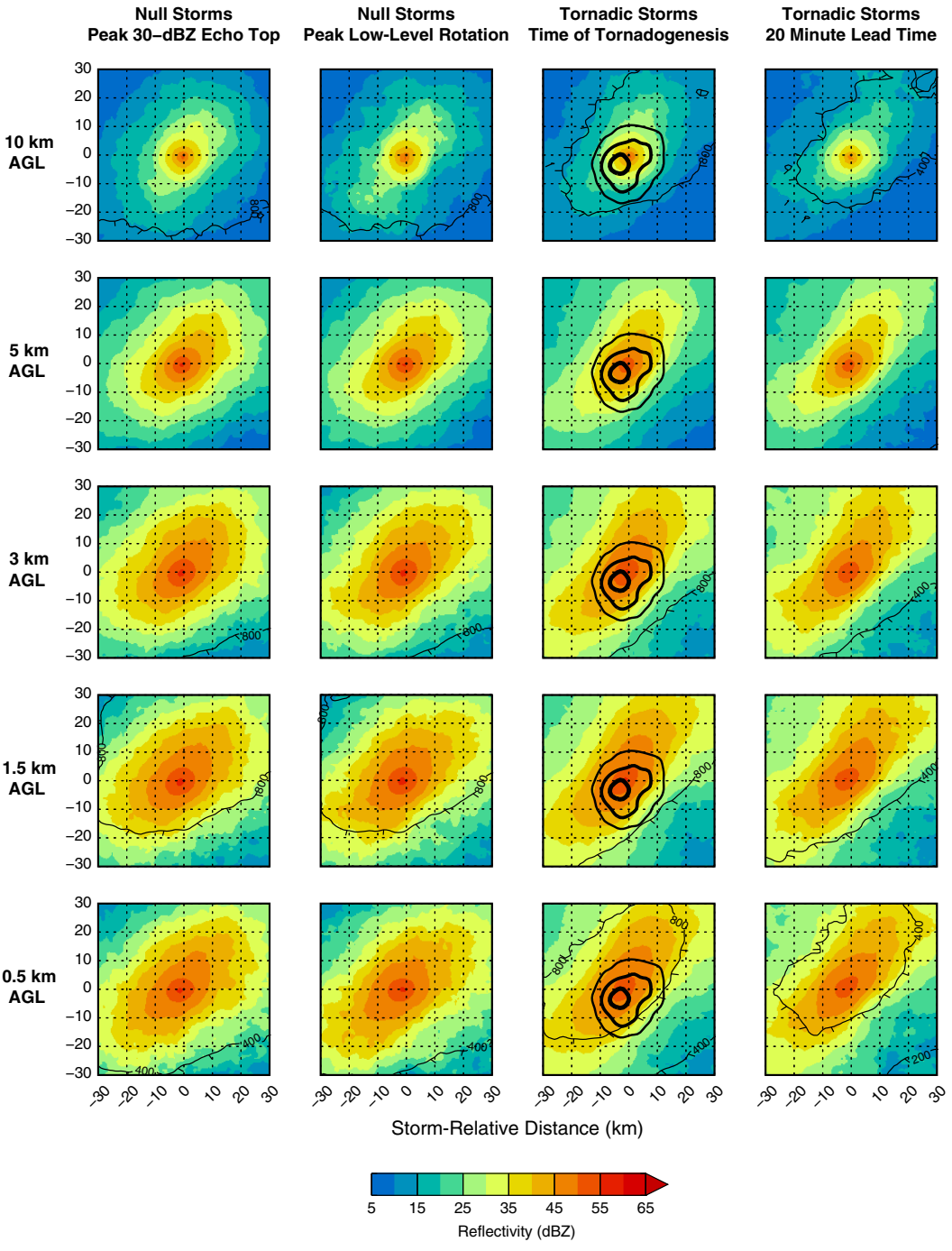

FIG. 3. PMM constant-altitude plots of Z_H for null and tornadic storms. Null data are shown for times of peak 30-dBZ echo-top height and peak low-level rotation, and tornadic data are shown at tornadogenesis and 20-min lead time. Data are shown at 0.5, 1.5, 3, 5, and 10 km AGL. Thin labeled contours represent the number of storms included in each mean, with dashes pointing toward lower values. Thicker contours represent total tornado reports (only in PMMs at time of tornadogenesis), with increasing contour thickness corresponding to higher frequency of reports. Contours enclose locations whose total report count is at least 30%, 60%, or 90% of the maximum density of reports (after Gaussian smoothing). Storm motion points to the right of each plot.

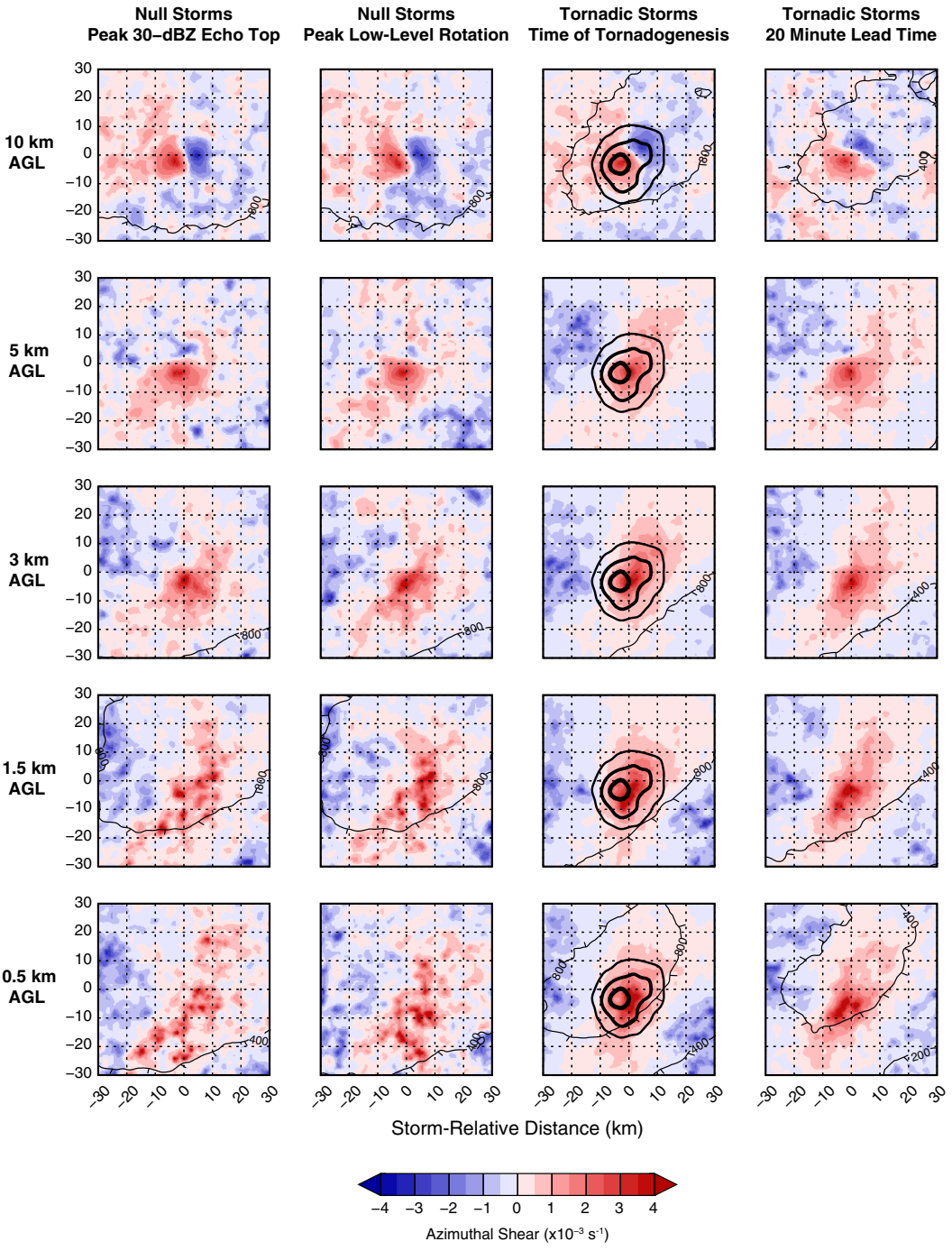

FIG. 4. As in Fig. 3, but for azimuthal shear.

storms, the location of the low-level mesovortex is in close proximity to the most frequent location of tornadogenesis and is overall collocated with the outermost tornadogenesis location contour. Distinct differences between azimuthal shear maxima and storm center are visible between the null and tornadic data. Throughout the majority of the storms' depths for tornadic storms at first tornadogenesis and 20 min prior, azimuthal shear maxima occur in a broadly consistent storm-relative location. Differences between tornadic and nontornadic cells are most evident at low levels, where low-level azimuthal shear maxima are less concentrated/coherent and displaced farther right of storm center and down-motion in nontornadic cells (i.e., less vertically aligned with upper-level mesovortex locations at 5–10 km). From 3 to 10 km, both types of storms show a dipole of positive/negative azimuthal shear, rotating roughly 90° clockwise in orientation

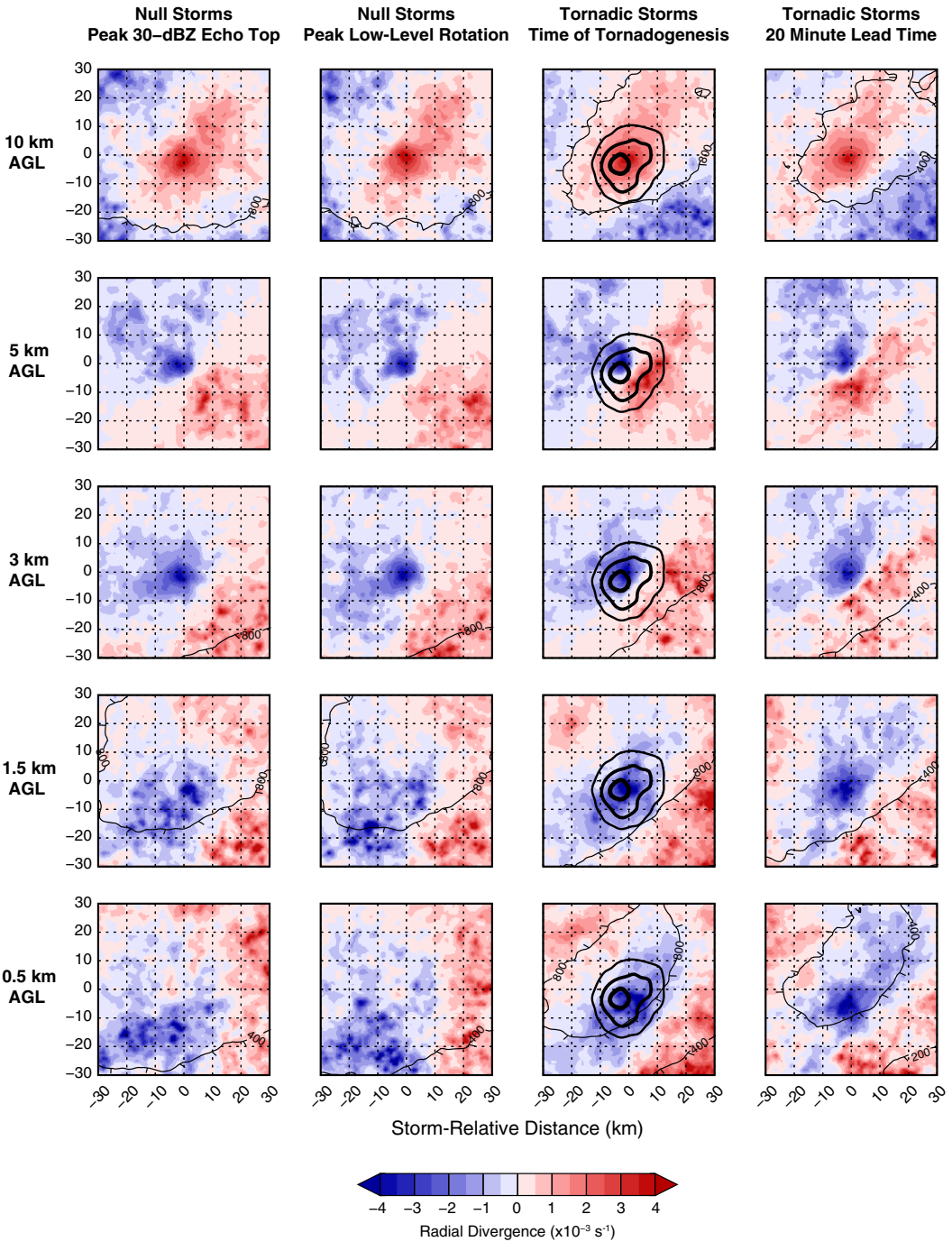

FIG. 5. As in Fig. 3, but for radial divergence.

through the column. Corresponding radial divergence PMMs in Fig. 5 show convergence (negative divergence) roughly collocated with tornadogenesis locations at 0.5 and 1.5 km, and convergence at the same altitudes within the null-storm PMMs is displaced right and up-motion relative to storm center. In both cases, low-level convergence signatures are roughly collocated with positive low-level azimuthal shear (Fig. 4). Looking at maximum convergence at 3 and 5 km and maximum divergence at 10 km, these signatures—indicative of the storm updraft's location—are close to storm center for both tornadic and null storms, as expected. This means that low-level vertical motion is better coupled with the mid- to upper-level storm updraft in tornadic cells than it is for the null cells. Figure 6 shows a near-collocation of enhanced σ_V values with storm center throughout the depth of tornadic storms, whereas such maxima are displaced from storm center

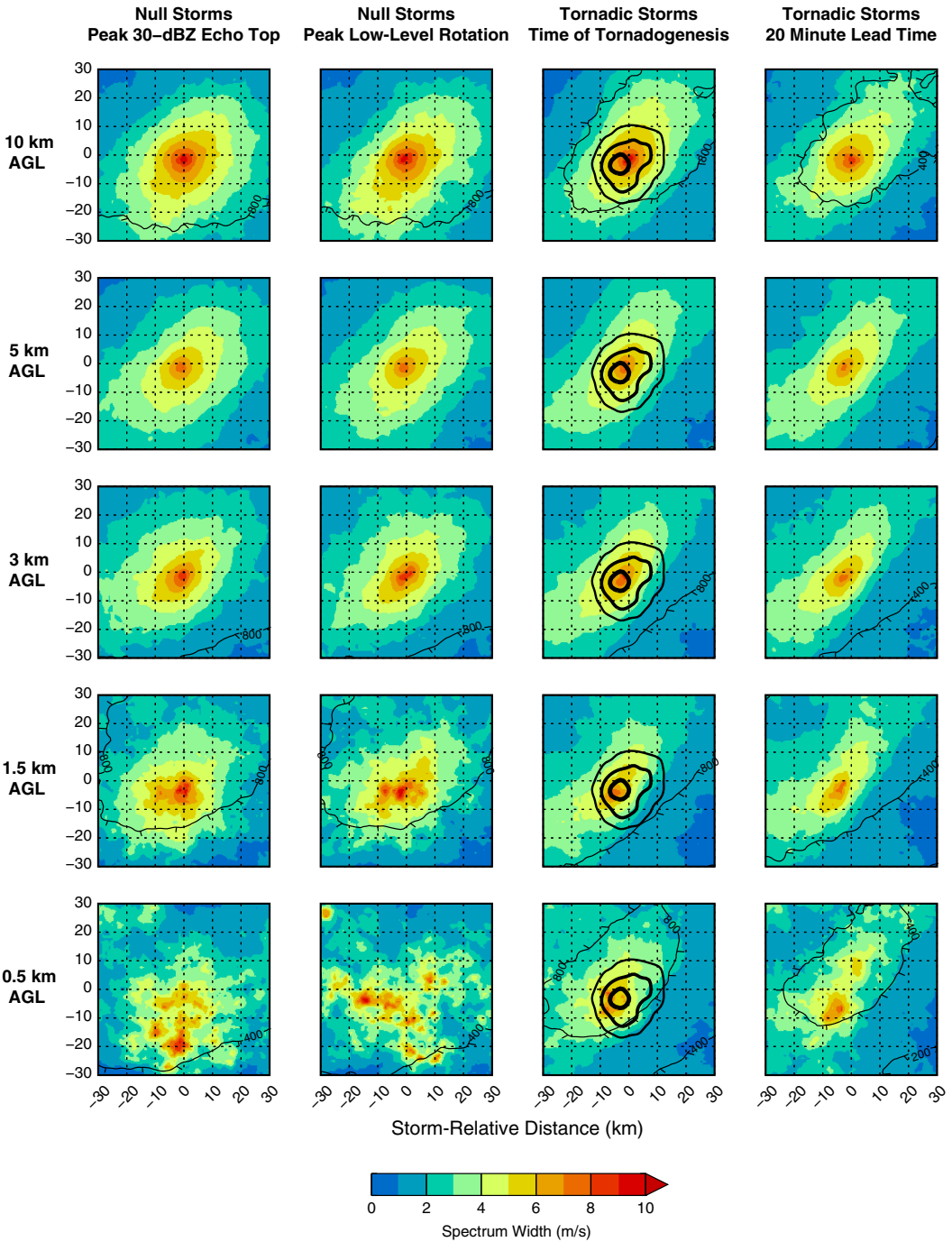

FIG. 6. As in Fig. 3, but for σ_V.

(and mid- to upper-level maxima) and less coherent at 0.5 km AGL for null storms. Magnitudes of low-level σ_V, however, are notably higher in nontornadic storms. Enhanced σ_V can be driven by several factors, including wind shear, rotation, and measurement error (e.g., Doviak and Zrnić 1993). Assessing the PMM fields in tandem, tornadic storms are marked by a collocation of low-level vertical vorticity, convergence, and enhanced σ_V with the mid- to upper-level updraft location. Conversely, these low-level features in null storms are more diffuse, less coupled with each other, and displaced from the mid- to upper-level updraft, impeding any stretching of the low-level rotation in the vertical and potential resultant tornadogenesis. It is important to note that the enhanced low-level azimuthal shear signature in tornadic storms stands out despite controlling for low-level azimuthal shear differences between tornadic and null storms via the null storm selection

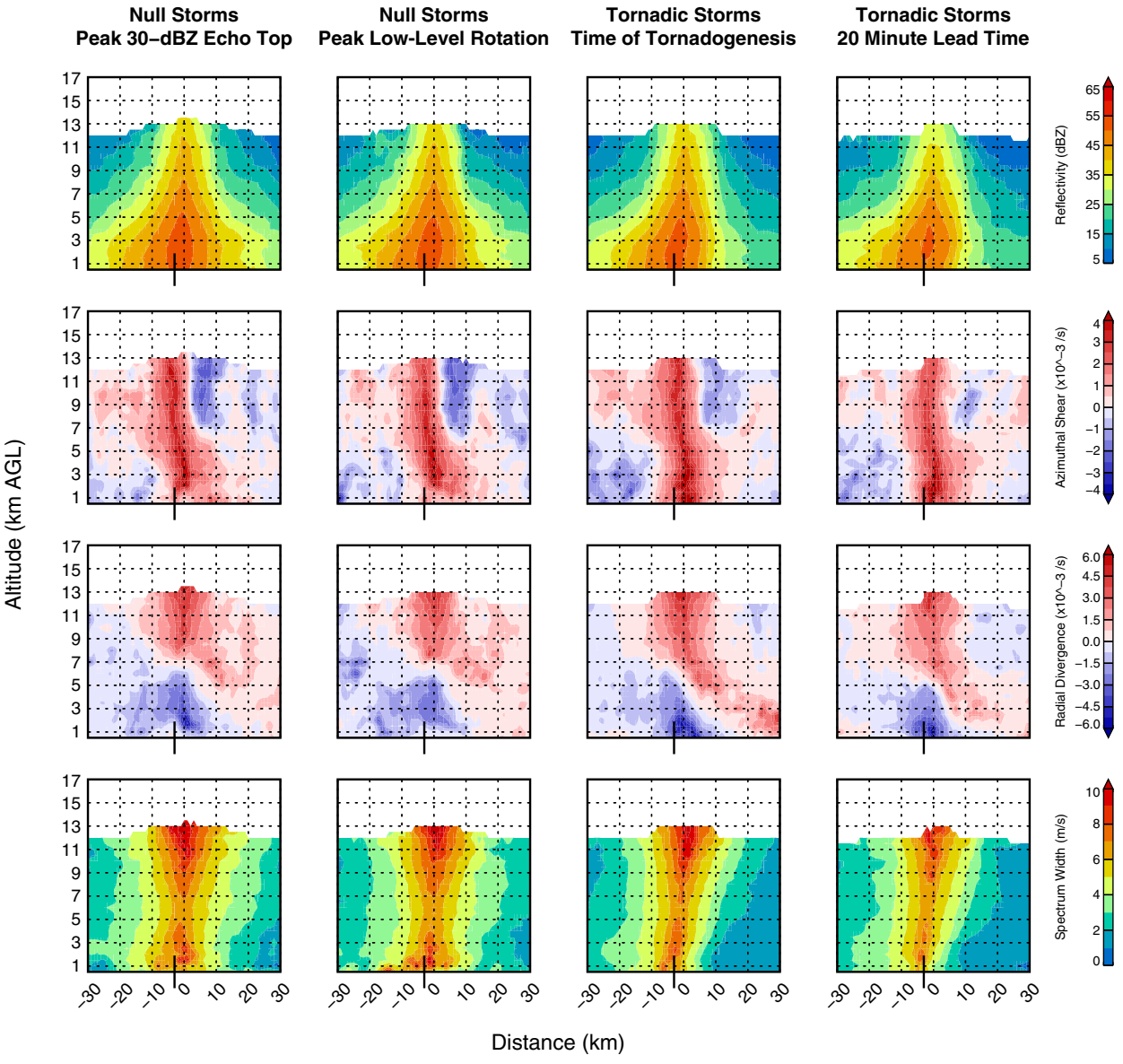

FIG. 7. Cross sections parallel to storm motion of PMM (top) Z_H, (top middle) azimuthal shear, (bottom middle) radial divergence, and (bottom) σ_V for (left),(left center) null and (right center),(right) tornadic storms. Null data are shown for times of peak 30-dBZ echo-top height and peak low-level rotation, and tornadic data are shown at tornadogenesis and 20-min lead time. Cross sections bisect the approximate maximum of tornado reports (see Fig. 4) with a center at (0, −3) km relative to storm updraft. Thick tick marks show the approximate location of the maximum in tornado report frequency.

criteria, highlighting the importance of taking into account both shear magnitude and location in assessing potentially tornadic nonsupercellular MCS storms.

Vertical PMM cross sections through tornadic and null storms offer additional insight into the storms' mean vertical structure beyond what can be inferred from individual constant-altitude PMMs. Figures 7 and 8 show cross sections through null and tornadic storms at the same times as Figs. 3–6, cutting through the storms both parallel to (Fig. 7) and perpendicular to (Fig. 8) storm motion. These cross sections are through the approximate frequency maximum in tornado reports (see Figs. 3–6) at (−3, −3) km relative to storm center. It is important to note that neither of these cross sections bisect storm center (and the approximate location of the mid to upper level updraft), so examinations here are focused on tornadogenesis-centered storm structure (or the equivalent storm-relative location in the case of null storms) rather than storm-centered structure, as was the case in Figs. 3–6.

A few storm characteristics are more evident from these vertical cross sections. Focusing on the parallel cross section in Fig. 7, a vertically aligned column of positive azimuthal shear indicating the mesovortex location is nearly coincident with

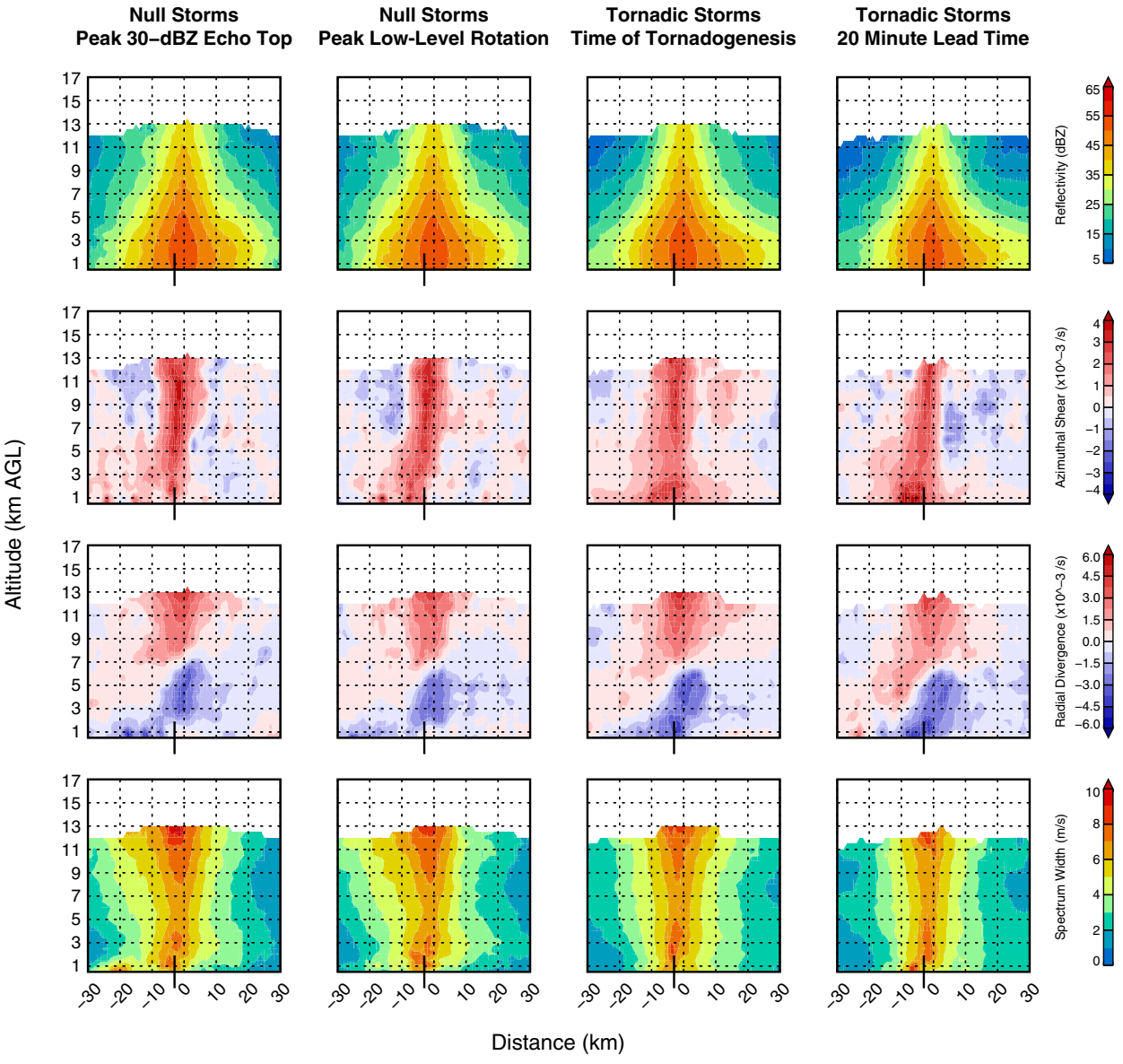

FIG. 8. As in Fig. 7, but taken perpendicular to storm motion. Cross sections bisect the approximate maximum of tornado reports (see Fig. 4) with a center at (−3, 0) km relative to storm updraft.

the most frequent tornadogenesis location in tornadic storms, whereas in null storms, the low-level mesovortex is displaced down-motion of the preferred tornadogenesis location and is no longer vertically aligned with the upper-level mesovortex location (which presents similar to that in tornadic cells). Divergence plots also show higher convergence at the lowest observed levels for tornadic cells, with low-level convergence in null cells approaching zero. From the cross sections perpendicular to storm motion (Fig. 8), both tornadic and null cases show enhanced azimuthal shear at low levels over the preferred tornadogenesis location, although the maxima for tornadic storms are more broadly distributed about the tornadogenesis location. Similar to Fig. 7, divergence plots show stronger convergence at the lowest levels for tornadic data than for null data, and σ_V behavior mirrors that of Fig. 7. Overall, it appears that the most critical characteristics of a tornadic cell are the vertical alignment of the mesovortex coupled with coincident enhanced low-level convergence (i.e., a strong low-level updraft coupled with the mid and upper level storm updraft). This association of enhanced rotation on radar with potential QLCS tornadogenesis has been noted before, including as a "confidence builder" in the three-ingredients method for identifying potential QLCS mesovortexgenesis and tornadogenesis (e.g., Gibbs 2021).

b. *Dual polarization*

Given the nationwide upgrade of all WSR-88D instruments to polarimetric capabilities by 2013, PMMs of polarimetric

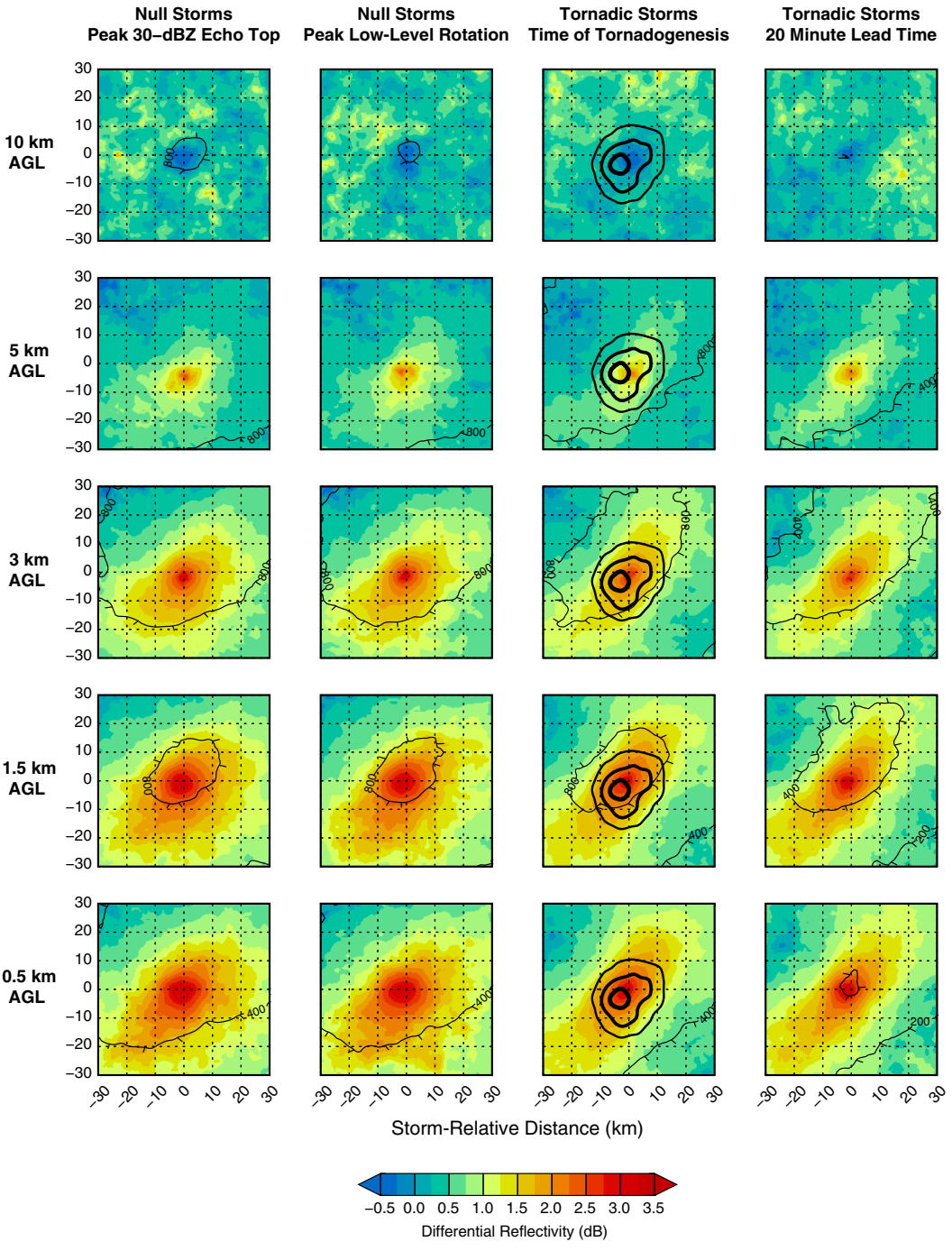

FIG. 9. As in Fig. 3, but for Z_{DR}.

radar data can also be examined to identify potential distinguishing microphysical characteristics. Figures 9–11 show constant-altitude PMMs for Z_{DR}, K_{DP}, and ρ_{HV}, respectively. Examining these figures together, there are two main differences that are evident between null and tornadic storms. The first difference is the orientation of storm motion relative to the broader MCS convective line orientation (as seen in PMMs of Z_H in Fig. 3). Namely, Figs. 9 and 10 show a preferential line orientation at ~45° left of storm motion at low levels for tornadic storms, and a more diffuse orientation for null storms. Second, all figures show slight differences between magnitudes of low-level Z_{DR} and K_{DP} maxima. For Z_{DR}, the maxima for tornadic and null storms (as shown by plotted contours) are the same, although contours of null-storm maxima cover a broader area. For K_{DP}, maxima are also the same, from 0.5 to 3 km across all storm types and

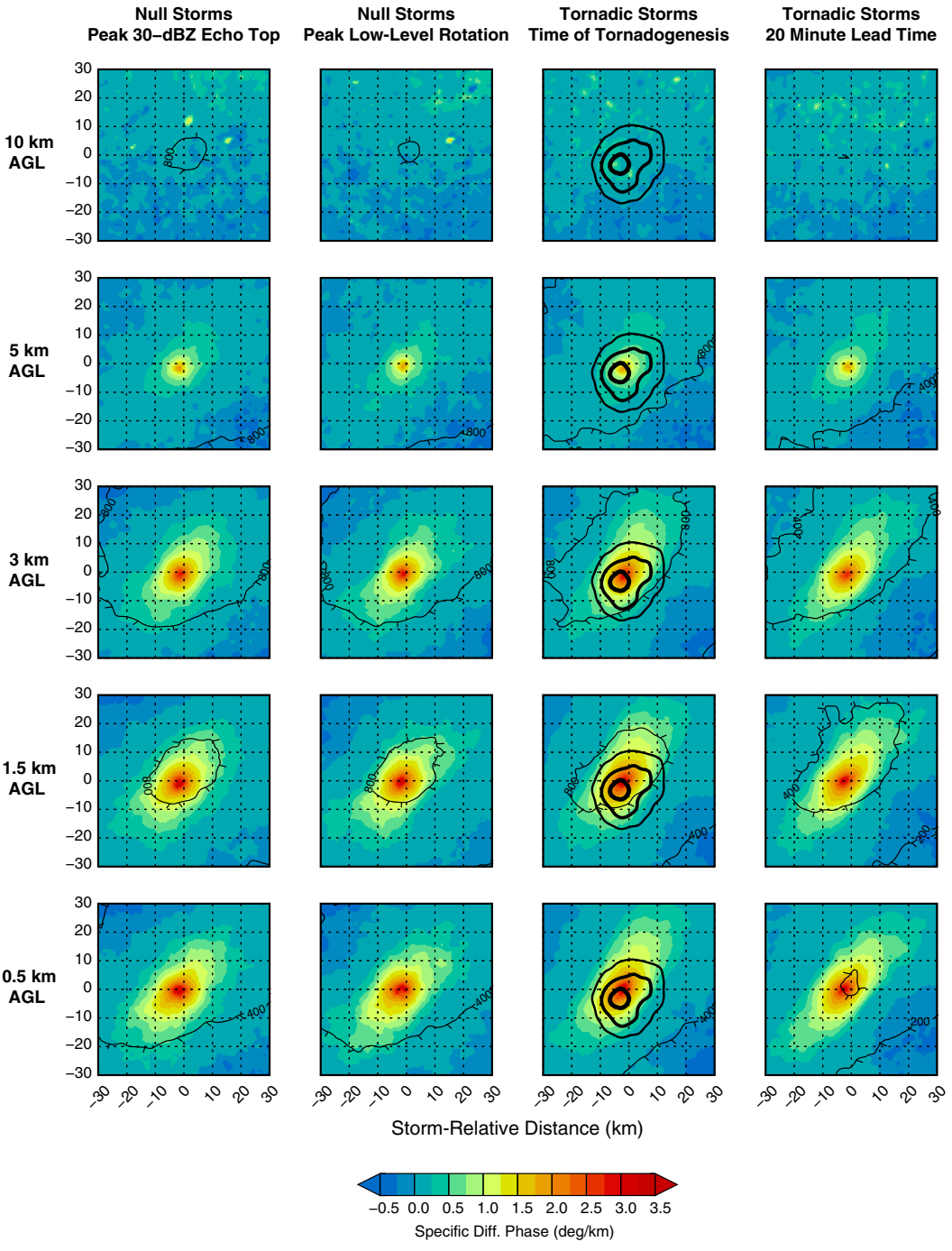

FIG. 10. As in Fig. 3, but for K_{DP}.

times, but this time, the maximum contours at first tornadogenesis cover a larger area (although less pronounced than the relative sizes of the Z_{DR} maximum contours). This may suggest a slight tendency toward a lower concentration of larger drops in null storms and a higher concentration of more moderately sized drops near time of tornadogenesis; however, Z_{DR} and K_{DP} values for null and tornadic storms are overall comparable. For ρ_{HV}, minimum values are comparable between PMMs and show no consistent differences between storm type.

Figures 12 and 13 show vertical cross sections of the polarimetric variables' PMMs through tornadic and null storms parallel and perpendicular to storm motion, respectively. Similar to Figs. 7 and 8, cross sections are through the preferred tornadogenesis location. Consistent with the constant-altitude plots, there are slight differences, but tornadic and null values are again mostly

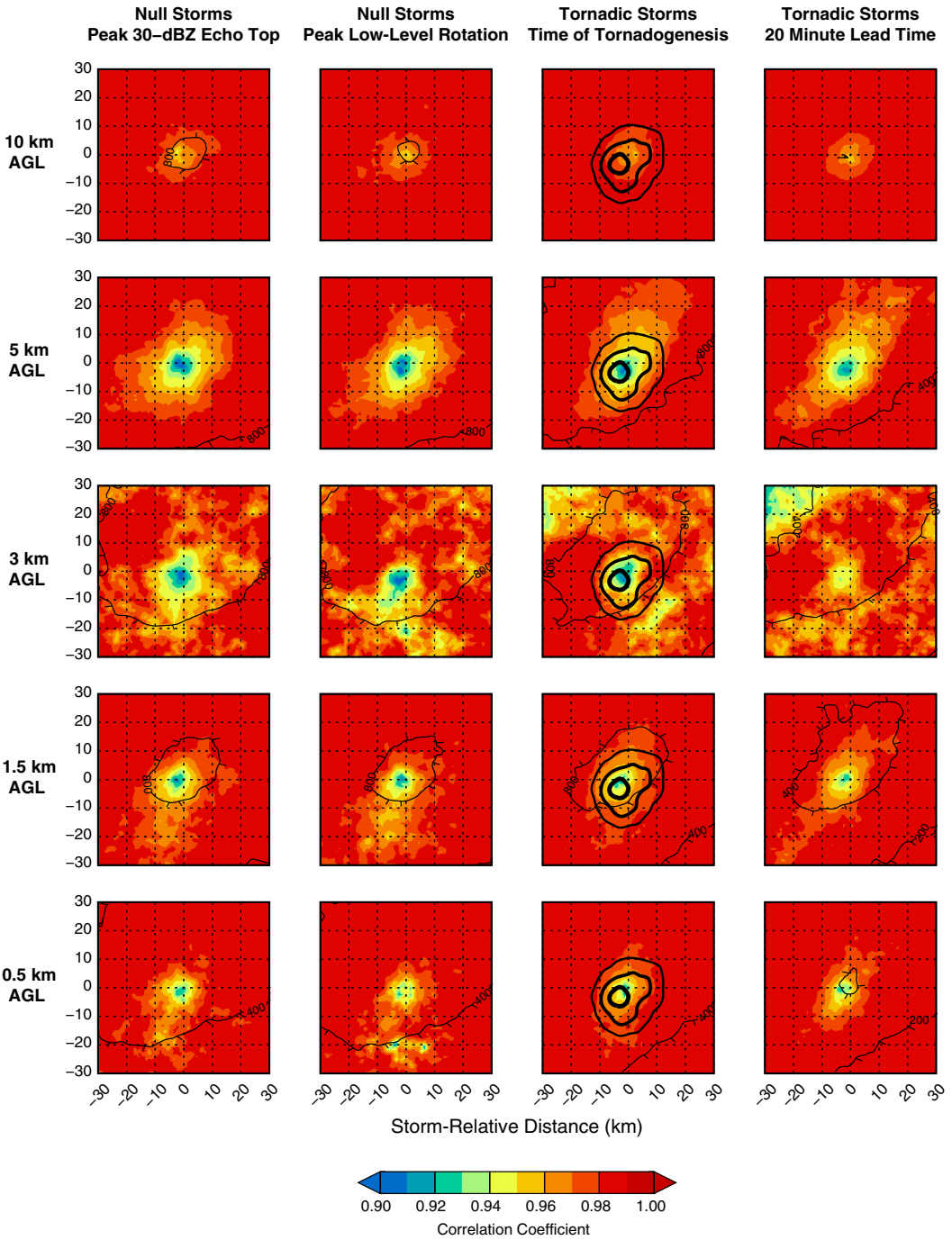

FIG. 11. As in Fig. 3, but for ρ_{HV}.

indistinguishable. Microphysically, higher Z_{DR} in null storms suggests larger drops near the surface as compared with smaller drops in tornadic storms. The melting layer (as deduced from local minima in ρ_{HV} away from the composite storms' convective cores) is comparable at 3–4 km AGL in both storm populations, so any differences owing to environmental variability are likely to have a limited impact on interpretation herein. Qualitatively, it appears that the more striking differences between the null and tornadic storms are seen in the single-polarization analyses, and polarimetric data provide limited additional discriminating information between nonsupercellular tornadic and nontornadic storms within MCSs.

4. Conclusions and discussion

This study examined the radar appearance of tornadic and nontornadic nonsupercell MCS storm cells, focusing on

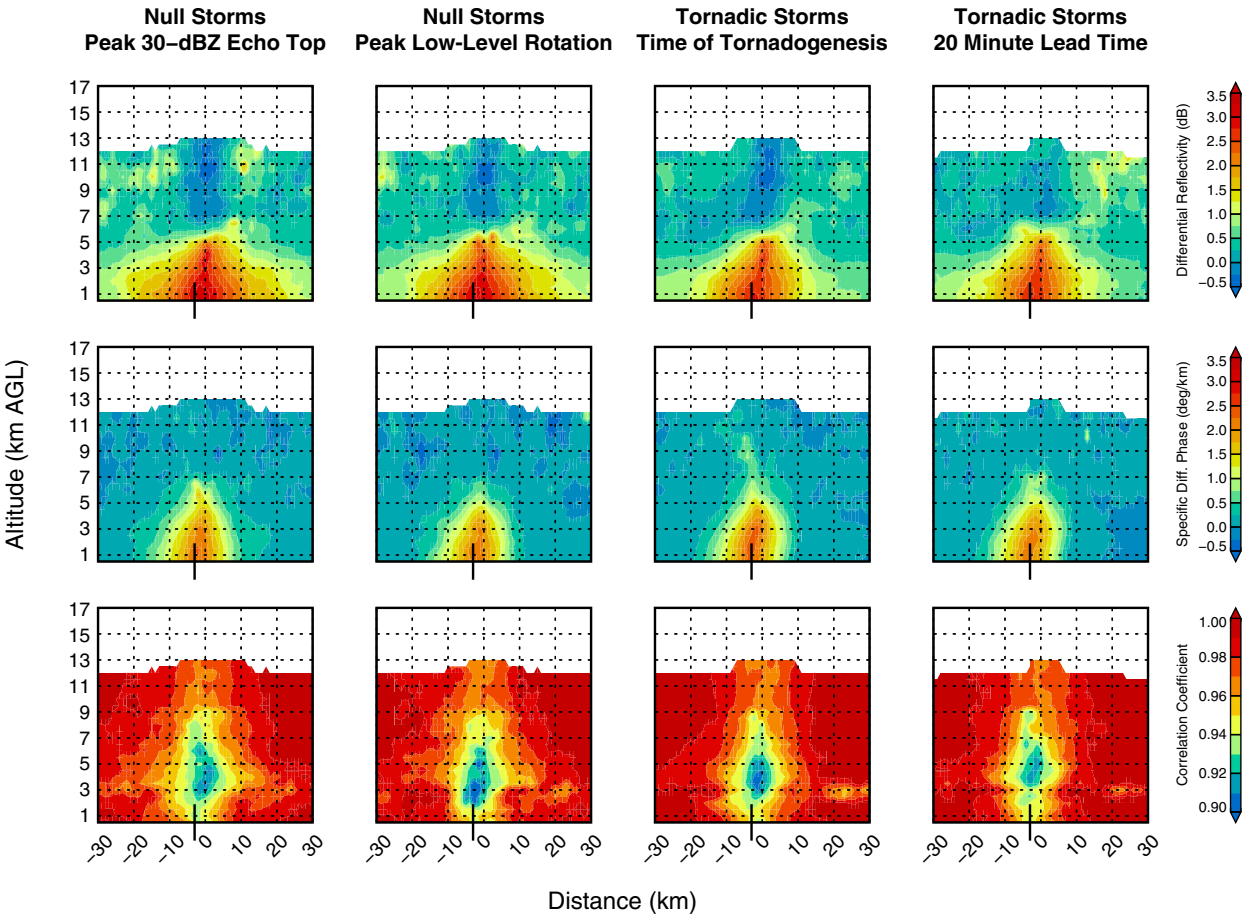

FIG. 12. As in Fig. 7, but examining (top) Z_{DR}, (middle) K_{DP}, and (bottom) ρ_{HV}.

nontornadic storms that otherwise look favorable for tornadogenesis (i.e., the null population). The major conclusions of this work are the following:

1) Comparisons of tornadic and nontornadic kinematic characteristics show that low-level, midlevel, and column-maximum azimuthal shear, as well as low-level divergence, have the greatest quantitative difference (as measured by K–S tests) between the tornadic and nontornadic storm populations. Focusing on low-level azimuthal shear values, null storms were randomly selected such that the distribution of null low-level azimuthal shear values matched the distribution of tornadic values. Sensitivity tests showed no meaningful differences in the distribution of tornadic and null values of other kinematic quantities based on the random sample. This resulted in 1627 tornadic and 1625 nontornadic (null) storms retained for analysis.
2) Analyzing PMM data at constant altitudes above ground level, Z_H, Z_{DR}, and K_{DP} data show a more concentrated lower-left to upper-right (relative to storm motion) axis for tornadic storms relative to null storms, potentially indicating a preferred storm motion-relative orientation for MCS line structures containing tornadic cells.
3) Comparing the kinematic characteristics of tornadic and null storms, much of the difference arises in the vertical alignment of low-level features conducive to stretching of vertical vorticity by the parent storm's mid- to upper-level updraft. In tornadic storms, maxima of azimuthal shear (rotation) and convergence are collocated, such that low-level rotation can be advected/stretched into the vertical by the low-level updraft. Low-level signatures of vertical motion are collocated with the mid- to upper-level updraft, allowing for further intensification of vorticity stretching and creating a conducive environment for tornadogenesis. Null storms differ in that they are characterized by a more diffuse field of low-level positive azimuthal shear horizontally displaced from a similarly diffuse field of low-level convergence. These signatures are also displaced from the mid- to upper-level updraft, so even weak vertical tilting of vorticity at low levels is likely decoupled from the parent storm updraft, limiting tornadogenesis potential via stretching. Therefore, enhanced low-level convergence and azimuthal shear coincident with one another and with the parent storm updraft are likely strong single-polarization indicators of tornadic potential for MCS nonsupercellular storms. Low-level azimuthal shear appearing as a discriminating characteristic between tornadic and

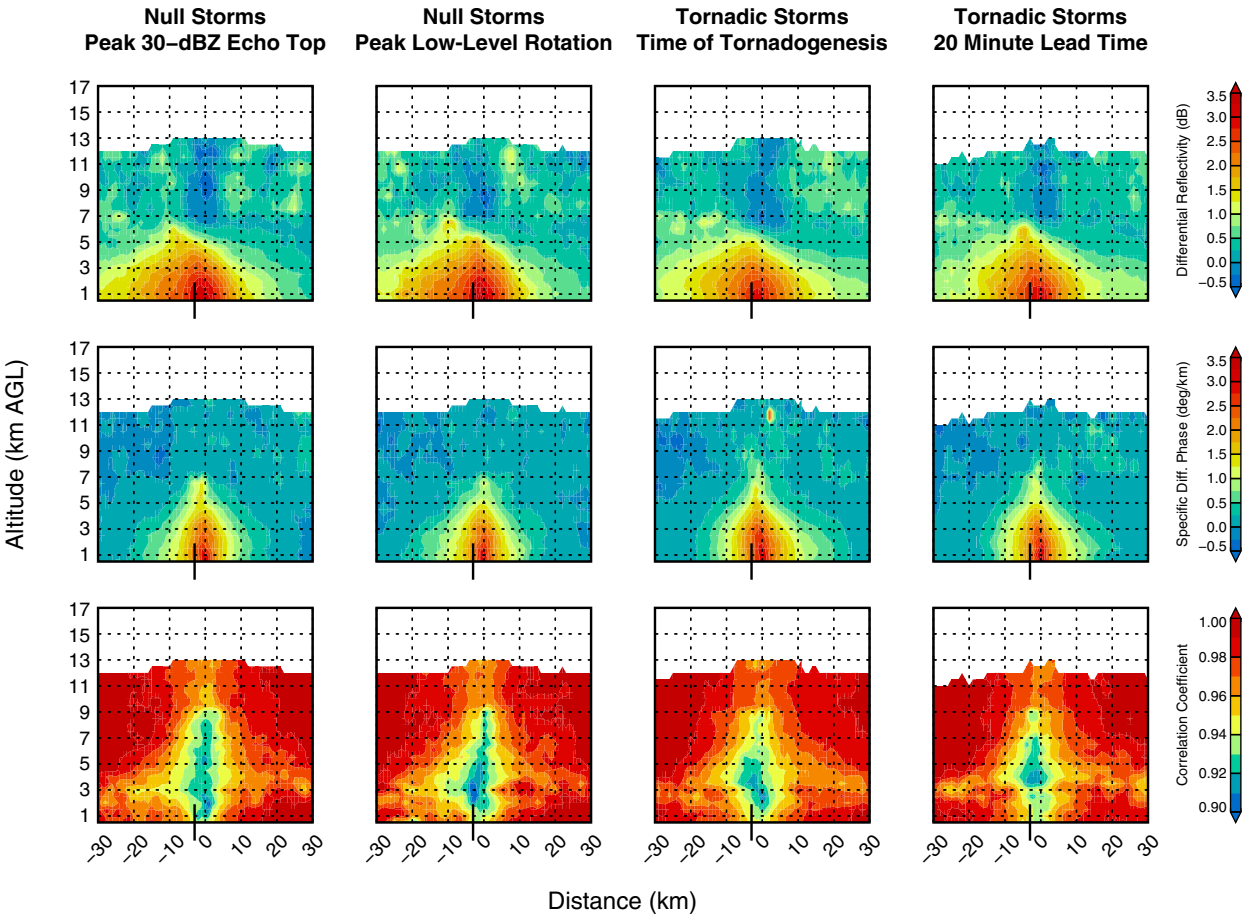

FIG. 13. As in Fig. 8, but examining (top) Z_{DR}, (middle) K_{DP}, and (bottom) ρ_{HV}.

null storms, despite using the distribution of low-level azimuthal shear values in tornadic storms to select the null population, emphasizes that not only the magnitude, but also the location of low-level azimuthal shear, is important for identifying potentially tornadic storms.

4) In contrast to single-polarization data, dual-polarization fields show little discriminating ability between tornadic and null MCS storms. The main differences between fields are with the storm's orientation relative to storm motion, which is also observable in Z_H data. For this reason, dual-polarization data offer little information beyond that available in single-polarization data to aid in identifying tornadic storms.

Given the strong, positive azimuthal shear collocated with the parent storm updraft at mid- to upper levels, concerns about contamination of the nonsupercellular MCS storm database with spurious (or many) supercell storms are warranted. Magnitudes between azimuthal shear values herein and those in PMM studies of supercells done by Homeyer et al. (2020) are comparable, but that is not particularly surprising; Weisman and Trapp (2003) note that QLCS mesovortices can be "similar in size and strength to mesocyclones associated with supercell storms." They also note that, despite this similarity, supercells are marked by long-lived and persistent midlevel rotation, whereas QLCS mesovortices are not. This is consistent with the supercell classification herein, where any storm that did not have maximum midlevel (4–7 km MSL) azimuthal shear exceeding 4×10^{-3} s^{-1} for at least 40 min was not classified as a supercell. Murphy et al. (2023) used the GR-S dataset to compare tornadic MCS nonsupercellular storms with the results of past studies that used manually selected tornadic MCS storms. Those comparisons found that the GR-S tornadic nonsupercellular MCS storms compared closely to the manually identified tornadic MCS storms, and GR-S tornadic supercellular MCS storms had characteristics more consistent with tornadic traditional supercells. For these reasons, we are confident that the nonsupercellular MCS population examined herein is not adversely impacted by contamination from supercellular storms.

Analyses herein show that probability-matched mean radar data, particularly single-polarization data, reveal key low- to midlevel features that can be used to discriminate between tornadic and nontornadic storms. These statistical results may be useful in improving warning decision-making practices for forecasters, since we find unique kinematic signatures that persist at long lead times to tornadogenesis in tornadic storms

and differ considerably in comparable nontornadic storms. Given that a vertically aligned rotating updraft is a major indicator of tornadic potential in storms analyzed herein, three-dimensional mesovortex evaluation in future high-resolution case studies of these events will be important to validate the perceived importance of low- to midlevel updraft alignment in nonmesocyclonic tornadogenesis. This result is particularly notable in that it agrees with comparable prior work focused solely on supercell storms (Homeyer et al. 2020), which suggests that vertical alignment of rotation and the low- to midlevel updraft are common requirements of tornadic storms regardless of storm mode. In addition, novel predictive methods such as artificial intelligence may benefit from focusing on the vertical alignment of mesovortices in future studies to improve warning performance for nonsupercellular MCS tornadoes (or tornadoes in general), especially their POD.

Acknowledgments. The authors thank three anonymous reviewers for their thoughtful, constructive, and kind comments that greatly improved the quality of the paper. Figures herein were designed to be equally interpretable to individuals with full color vision and individuals with color vision deficiency. This material is based upon work supported by the National Science Foundation under Grant ICER-2019758. This work is part of the NSF AI Institute for Research on Trustworthy AI in Weather, Climate, and Coastal Oceanography (AI2ES).

Data availability statement. Radar data are publicly accessible through the National Centers for Environmental Information (NOAA/NWS/ROC 1991), and storm reports can be accessed from the Storm Events Database (NOAA/NCEI 2022). GR-S data are publicly available via the Research Data Archive at the National Center for Atmospheric Research Computational and Information Systems Laboratory (School of Meteorology, University of Oklahoma 2021).

REFERENCES

Agee, E., and E. Jones, 2009: Proposed conceptual taxonomy for proper identification and classification of tornado events. *Wea. Forecasting*, **24**, 609–617, https://doi.org/10.1175/2008WAF2222163.1.

Amburn, S. A., and P. L. Wolf, 1997: VIL density as a hail indicator. *Wea. Forecasting*, **12**, 473–478, https://doi.org/10.1175/1520-0434(1997)012<0473:VDAAHI>2.0.CO;2.

Anderson-Frey, A. K., and H. Brooks, 2021: Compared to what? Establishing environmental baselines for tornado warning skill. *Bull. Amer. Meteor. Soc.*, **102**, E738–E747, https://doi.org/10.1175/BAMS-D-19-0310.1.

——, Y. P. Richardson, A. R. Dean, R. L. Thompson, and B. T. Smith, 2016: Investigation of near-storm environments for tornado events and warnings. *Wea. Forecasting*, **31**, 1771–1790, https://doi.org/10.1175/WAF-D-16-0046.1.

Ashley, W. S., A. M. Haberlie, and J. Strohm, 2019: A climatology of quasi-linear convective systems and their hazards in the United States. *Wea. Forecasting*, **34**, 1605–1631, https://doi.org/10.1175/WAF-D-19-0014.1.

Aydin, K., T. A. Seliga, and V. Balaji, 1986: Remote sensing of hail with a dual linear polarization radar. *J. Climate Appl. Meteor.*, **25**, 1475–1484, https://doi.org/10.1175/1520-0450(1986)025<1475:RSOHWA>2.0.CO;2.

Brooks, H. E., and J. Correia Jr., 2018: Long-term performance metrics for National Weather Service tornado warnings. *Wea. Forecasting*, **33**, 1501–1511, https://doi.org/10.1175/WAF-D-18-0120.1.

Brotzge, J. A., S. E. Nelson, R. L. Thompson, and B. T. Smith, 2013: Tornado probability of detection and lead time as a function of convective mode and environmental parameters. *Wea. Forecasting*, **28**, 1261–1276, https://doi.org/10.1175/WAF-D-12-00119.1.

Coffer, B. E., M. D. Parker, R. L. Thompson, B. T. Smith, and R. E. Jewell, 2019: Using near-ground storm relative helicity in supercell tornado forecasting. *Wea. Forecasting*, **34**, 1417–1435, https://doi.org/10.1175/WAF-D-19-0115.1.

Coniglio, M. C., and R. E. Jewell, 2022: SPC mesoscale analysis compared to field-project soundings: Implications for supercell environment studies. *Mon. Wea. Rev.*, **150**, 567–588, https://doi.org/10.1175/MWR-D-21-0222.1.

Crum, T. D., and R. L. Alberty, 1993: The WSR-88D and the WSR-88D operational support facility. *Bull. Amer. Meteor. Soc.*, **74**, 1669–1688, https://doi.org/10.1175/1520-0477(1993)074<1669:TWATWO>2.0.CO;2.

Doviak, R. J., and D. S. Zrnić, 1993: *Doppler Radar and Weather Observations*. 2nd ed. Academic Press, 562 pp.

Ebert, E. E., 2001: Ability of a poor man's ensemble to predict the probability and distribution of precipitation. *Mon. Wea. Rev.*, **129**, 2461–2480, https://doi.org/10.1175/1520-0493(2001)129<2461:AOAPMS>2.0.CO;2.

Ernst, S., J. Ripberger, M. J. Krocak, H. Jenkins-Smith, and C. Silva, 2021: Colorful language: Investigating public interpretation of the Storm Prediction Center convective outlook. *Wea. Forecasting*, **36**, 1785–1797, https://doi.org/10.1175/WAF-D-21-0001.1.

Flournoy, M. D., and M. C. Coniglio, 2019: Origins of vorticity in a simulated tornadic mesovortex observed during PECAN on 6 July 2015. *Mon. Wea. Rev.*, **147**, 107–134, https://doi.org/10.1175/MWR-D-18-0221.1.

Gibbs, J. G., 2021: Evaluating precursor signals for QLCS tornado and higher impact straight-line wind events. *J. Oper. Meteor.*, **9**, 62–75, https://doi.org/10.15191/nwajom.2021.0905.

Greene, D. R., and R. A. Clark, 1972: Vertically integrated liquid water—A new analysis tool. *Mon. Wea. Rev.*, **100**, 548–552, https://doi.org/10.1175/1520-0493(1972)100<0548:VILWNA>2.3.CO;2.

Hoekstra, S., K. Klockow, R. Riley, J. Brotzge, H. Brooks, and S. Erickson, 2011: A preliminary look at the social perspective of warn-on-forecast: Preferred tornado warning lead time and the general public's perceptions of weather risks. *Wea. Climate Soc.*, **3**, 128–140, https://doi.org/10.1175/2011WCAS1076.1.

Homeyer, C. R., T. N. Sandmæl, C. K. Potvin, and A. M. Murphy, 2020: Distinguishing characteristics of tornadic and nontornadic supercell storms from composite mean analyses of radar observations. *Mon. Wea. Rev.*, **148**, 5015–5040, https://doi.org/10.1175/MWR-D-20-0136.1.

——, E. M. Murillo, and M. R. Kumjian, 2023: Relationships between 10 years of radar-observed supercell characteristics and hail potential. *Mon. Wea. Rev.*, **151**, 2609–2632, https://doi.org/10.1175/MWR-D-23-0019.1.

Krocak, M. J., J. N. Allan, J. T. Ripberger, C. L. Silva, and H. C. Jenkins-Smith, 2021: An analysis of tornado warning reception

and response across time: Leveraging respondents' confidence and a nocturnal tornado climatology. *Wea. Forecasting*, **36**, 1649–1660, https://doi.org/10.1175/WAF-D-20-0207.1.

Loeffler, S. D., and M. R. Kumjian, 2018: Quantifying the separation of enhanced Z_{DR} and K_{DP} regions in nonsupercell tornadic storms. *Wea. Forecasting*, **33**, 1143–1157, https://doi.org/10.1175/WAF-D-18-0011.1.

Lyza, A. W., M. D. Flournoy, and E. N. Rasmussen, 2022: Observed characteristics of the tornadic supercells of 27–28 April 2011 in the southeast United States. *Mon. Wea. Rev.*, **150**, 2883–2910, https://doi.org/10.1175/MWR-D-21-0274.1.

Markowski, P. M., and Y. P. Richardson, 2009: Tornadogenesis: Our current understanding, forecasting considerations, and questions to guide future research. *Atmos. Res.*, **93**, 3–10, https://doi.org/10.1016/j.atmosres.2008.09.015.

Mason, L. R., K. N. Ellis, B. Winchester, and S. Schexnayder, 2018: Tornado warnings at night: Who gets the message? *Wea. Climate Soc.*, **10**, 561–568, https://doi.org/10.1175/WCAS-D-17-0114.1.

Murphy, A. M., C. R. Homeyer, and K. Q. Allen, 2023: Development and investigation of GridRad-Severe, a multi-year severe event radar dataset. *Mon. Wea. Rev.*, **151**, 2257–2277, https://doi.org/10.1175/MWR-D-23-0017.1.

NOAA/NCEI, 2022: NOAA's storm events database. National Centers for Environmental Information, accessed 31 January 2022, https://www.ncdc.noaa.gov/stormevents/.

NOAA/NWS/ROC, 1991: NOAA Next Generation Radar (NEXRAD) level 2 base data. National Centers for Environmental Information, accessed 31 January 2022, ncei.noaa.gov/access/metadata/landing-page/bin/iso?id=gov.noaa.ncdc:C00345.

Ripberger, J. T., M. J. Krocak, W. W. Wehde, J. N. Allan, C. Silva, and H. Jenkins-Smith, 2019: Measuring tornado warning reception, comprehension, and response in the United States. *Wea. Climate Soc.*, **11**, 863–880, https://doi.org/10.1175/WCAS-D-19-0015.1.

Rotunno, R., J. B. Klemp, and M. L. Weisman, 1988: A theory for strong, long-lived squall lines. *J. Atmos. Sci.*, **45**, 463–485, https://doi.org/10.1175/1520-0469(1988)045<0463:ATFSLL>2.0.CO;2.

Sandmæl, T. N., 2017: An evaluation of radar- and satellite-data based products to discriminate between tornadic and non-tornadic storms. M.S. thesis, Dept. of Meteorology, University of Oklahoma, 98 pp.

Schaefer, J. T., 1990: The critical success index as an indicator of warning skill. *Wea. Forecasting*, **5**, 570–575, https://doi.org/10.1175/1520-0434(1990)005<0570:TCSIAA>2.0.CO;2.

School of Meteorology, University of Oklahoma, 2021: GridRad-Severe—Three-dimensional gridded NEXRAD WSR-88D radar data for severe events. Accessed 17 April 2023, https://doi.org/10.5065/2B46-1A97.

Skinner, P. S., and Coauthors, 2018: Object-based verification of a prototype warn-on-forecast system. *Wea. Forecasting*, **33**, 1225–1250, https://doi.org/10.1175/WAF-D-18-0020.1.

Stensrud, D. J., and Coauthors, 2009: Convective-scale warn-on-forecast system: A vision for 2020. *Bull. Amer. Meteor. Soc.*, **90**, 1487–1500, https://doi.org/10.1175/2009BAMS2795.1.

——, and Coauthors, 2013: Progress and challenges with warn-on-forecast. *Atmos. Res.*, **123**, 2–16, https://doi.org/10.1016/j.atmosres.2012.04.004.

Taszarek, M., N. Pilguj, J. T. Allen, V. Gensini, H. E. Brooks, and P. Szuster, 2021: Comparison of convective parameters derived from ERA5 and MERRA-2 with rawinsonde data over Europe and North America. *J. Climate*, **34**, 3211–3237, https://doi.org/10.1175/JCLI-D-20-0484.1.

Thompson, R. L., B. T. Smith, J. S. Grams, A. R. Dean, and C. Broyles, 2012: Convective modes for significant severe thunderstorms in the contiguous United States. Part II: Supercell and QLCS tornado environments. *Wea. Forecasting*, **27**, 1136–1154, https://doi.org/10.1175/WAF-D-11-00116.1.

Trapp, R. J., and M. L. Weisman, 2003: Low-level mesovortices within squall lines and bow echoes. Part II: Their genesis and implications. *Mon. Wea. Rev.*, **131**, 2804–2823, https://doi.org/10.1175/1520-0493(2003)131<2804:LMWSLA>2.0.CO;2.

——, S. A. Tessendorf, E. S. Godfrey, and H. E. Brooks, 2005: Tornadoes from squall lines and bow echoes. Part I: Climatological distribution. *Wea. Forecasting*, **20**, 23–34, https://doi.org/10.1175/WAF-835.1.

Trujillo-Falcón, J. E., O. Bermúdez, K. Negrón-Hernández, J. Lipski, E. Leitman, and K. Berry, 2021: Hazardous weather communication en español: Challenges, current resources, and future practices. *Bull. Amer. Meteor. Soc.*, **102**, E765–E773, https://doi.org/10.1175/BAMS-D-20-0249.1.

Uccellini, L. W., and J. E. T. Ten Hoeve, 2019: Evolving the National Weather Service to build a weather-ready nation: Connecting observations, forecasts, and warnings to decision-makers through impact-based decision support services. *Bull. Amer. Meteor. Soc.*, **100**, 1923–1942, https://doi.org/10.1175/BAMS-D-18-0159.1.

Weisman, M. L., and C. A. Davis, 1998: Mechanisms for the generation of mesoscale vortices within quasi-linear convective systems. *J. Atmos. Sci.*, **55**, 2603–2622, https://doi.org/10.1175/1520-0469(1998)055<2603:MFTGOM>2.0.CO;2.

——, and R. J. Trapp, 2003: Low-level mesovortices within squall lines and bow echoes. Part I: Overview and dependence on environmental shear. *Mon. Wea. Rev.*, **131**, 2779–2803, https://doi.org/10.1175/1520-0493(2003)131<2779:LMWSLA>2.0.CO;2.